



CHORUS

This is the accepted manuscript made available via CHORUS. The article has been published as:

Rheology of sediment transported by a laminar flow

M. Houssais, C. P. Ortiz, D. J. Durian, and D. J. Jerolmack

Phys. Rev. E **94**, 062609 — Published 19 December 2016

DOI: [10.1103/PhysRevE.94.062609](https://doi.org/10.1103/PhysRevE.94.062609)

Rheology of sediment transported by a laminar flow*

M. Houssais[†]

*Department of Earth and Environmental Science,
University of Pennsylvania, Philadelphia, Pennsylvania 19104, USA. and
Levich Institute, City College of CUNY, 140th Street and Convent Avenue, New York, NY 10031, USA.*

C. P. Ortiz

*Department of Earth and Environmental Science,
University of Pennsylvania, Philadelphia, Pennsylvania 19104, USA. and
Department of Physics and Astronomy, University of Pennsylvania, Philadelphia, Pennsylvania 19104, USA.*

D. J. Durian

Department of Physics and Astronomy, University of Pennsylvania, Philadelphia, Pennsylvania 19104, USA.

D. J. Jerolmack

*Department of Earth and Environmental Science,
University of Pennsylvania, Philadelphia, Pennsylvania 19104, USA.*

(Dated: November 23, 2016)

Understanding the dynamics of fluid-driven sediment transport remains challenging, as it occurs at the interface between a granular material and a fluid flow. Boyer, Guazzelli, and Pouliquen [Phys. Rev. Lett. 107, 188301 (2011)] proposed a local rheology unifying dense dry-granular and viscous-suspension flows, but it has been validated only for neutrally-buoyant particles in a confined and homogeneous system. Here we generalize the Boyer, Guazzelli and Pouliquen model to account for the weight of a particle by addition of a pressure P_0 , and test the ability of this model to describe sediment transport in an idealized laboratory river. We subject a bed of settling plastic particles to a laminar-shear flow from above, and use Refractive-Index-Matching to track particles' motion and determine local rheology — from the fluid-granular interface to deep in the granular bed. Data from all experiments collapse onto a single curve of friction μ as a function of the viscous number I_v over the range $3 \times 10^{-5} \leq I_v \leq 2$, validating the local rheology model. For $I_v < 3 \times 10^{-5}$, however, data do not collapse. Instead of undergoing a jamming transition with $\mu \rightarrow \mu_s$ as expected, particles transition to a creeping regime where we observe a continuous decay of the friction coefficient $\mu \leq \mu_s$ as I_v decreases. The rheology of this creep regime cannot be described by the local model, and more work is needed to determine whether a non-local rheology model can be modified to account for our findings.

I. INTRODUCTION

Sediment transport involves the entrainment and movement of a granular material by a shearing fluid flow. Although natural fluid flows are turbulent, experiments have shown that laminar flows can produce similar behavior in terms of sediment transport and morphodynamics [1–4]. Until recently, researchers have emphasized the role of hydrodynamics: a fluid flow over a rough static bed develops a characteristic shear stress τ , which triggers the entrainment of grains at the bed surface above a critical value τ_c . Numerous experimental, analytical and field studies have shown that the value of τ_c depends on the particle Reynolds number and the bed-surface particle size distribution [5–9]. This work has been integral to the development of equations for predicting rates of sediment transport. Much research has focused on bed-load transport [10–12] — the movement of grains by rolling,

sliding and hopping along the sediment bed — because of its importance for shaping ripples and dunes [1, 13], and for determining stream channel geometry [14–16]. We identify, however, three major shortcomings to this approach. First, the processes of river bed-load and suspension transport, landslides and debris flows, and hillslope-soil creep are considered and studied separately. Yet, all of them involve the same components: movement of grains due to a tangential stress composed of gravity and flow shear. Second, the threshold of sediment transport has been observed to vary through time in experimental [1] and natural rivers [17, 18], violating the classical prediction of a unique τ_c value for a given system. Third, empirical sediment-transport laws notoriously break down as the shear stress enters the vicinity of the critical value τ_c [19].

Researchers have begun to recognize the importance of accounting for particle-particle interactions to correctly predict sediment entrainment by fluid flows [20–26]. In particular, analytical and experimental results from Aussillous *et al.* [23] stressed the need to incorporate granular rheology in two-phase modeling of sediment transport. Our previous work also suggested that the bed-load

* A footnote to the article title

[†] housais.morgane@gmail.com.

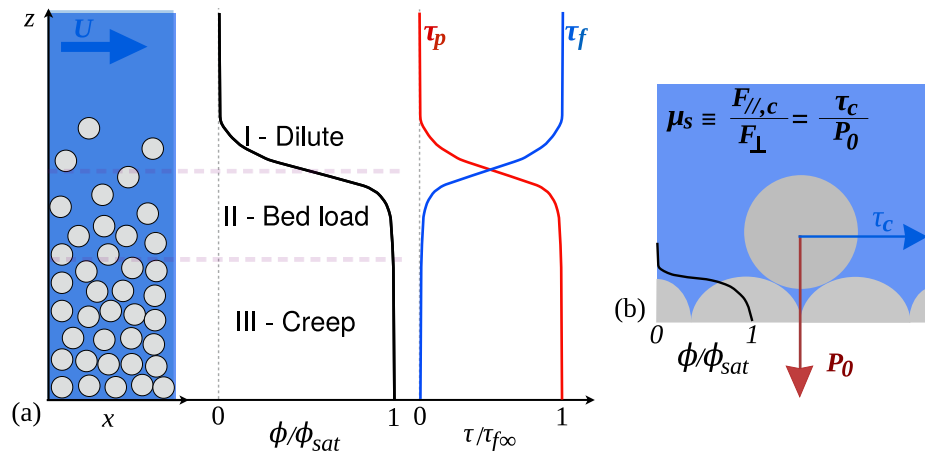


FIG. 1. Schematic representation of sediment transport. a) 2D sketch of sediment transport above the critical shear stress, $\tau > \tau_c$. From left to right (black, red and blue online) curves, respectively, show vertical trends of the packing fraction ϕ , the shear stress due to particles τ_p , and the shear stress associated with the fluid τ_f . $\tau_{f\infty}$ is the constant fluid-shear stress far from the particles. b) Schematic of entrainment of a single grain at the threshold of motion, on an idealized bed surface. In that case, by definition the friction coefficient is the static value μ_s , strictly equal to the ratio of the tangential force $F_{//,c}$ to the normal force F_{\perp} applied to the particle.

transport regime behaves as a dense granular flow [27]. These studies provide evidence that explicit consideration of the mechanics of granular materials may address the limitations of the classical sediment transport framework. In this paper, we test the ability of a local, submerged granular rheology model to describe the effective friction of fluid-driven particle motion – from very dense and slow to very dilute and fast.

Here, we consider the rheology of a granular medium under steady simple shear flow [28] satisfying $\nabla \cdot \tau = 0$, where the shear stress is $\tau = \eta_{\text{eff}} \dot{\gamma}$ where η_{eff} is the effective viscosity and $\dot{\gamma}$ is the local shear rate. Granular flows exhibit a nonlinear rheology: for dry systems, it has been established experimentally that the effective viscosity decreases as the local shear rate increases relative to the local confinement pressure P_p [29]. The rheology can be equivalently described using the effective viscosity or the effective friction coefficient $\mu = \frac{\tau}{P_p}$ as the material property controlling the stress [30], because $\tau = \mu P_p = \eta_{\text{eff}} \dot{\gamma}$.

It is also possible to equivalently write either η_{eff} or μ in terms of the solids packing fraction ϕ or a dimensionless timescale I [30]. Values for μ observed in sheared granular experiments collapse to a single function of a time-scale ratio $I = \frac{t_{\text{micro}}}{t_{\text{macro}}}$ (refs. 29, 31–33). Here $t_{\text{macro}} \equiv 1/\dot{\gamma}$ is the average macroscopic timescale of system deformation, and t_{micro} is the microscopic timescale for particle rearrangement in the pack due to the confinement pressure. The dominant timescales in I depend on the properties of the grains and surrounding fluid, and have been shown to depend principally on two other parameters: the ratio of particle and fluid densities ρ_p/ρ_f , and the Stokes number St [34, 35]. For the case of a granular material submerged in a fluid of viscosity η_f , in the limit $\rho_p/\rho_f \simeq 1$ and $St < 1$, t_{micro} is driven by viscous drag; therefore dimensional analysis leads to $t_{\text{micro}} = \eta_f/P_p$.

The appropriate time scale ratio I in this limit has been defined as the viscous number I_v [34, 35]:

$$I_v = \frac{\eta_f |\dot{\gamma}|}{P_p}. \quad (1)$$

In the submerged case under simple shear, the shear stress τ is carried by fluid and particle motion, $\tau = \tau_p + \tau_f$, but the exchange of stress between the two phases occurs within a particle diameter of encountering the bed, (see schematic in Fig. 1). It is then possible to define a total effective friction coefficient μ resulting from the sum of the particle-particle and particle-fluid interactions. Boyer *et al.* [30] conducted a novel set of simple shear experiments which determined the relationship $\mu(I_v)$ for the case of neutrally-buoyant particles ($\rho_p/\rho_f = 1$) immersed in a viscous fluid. By controlling the shear stress and also the confining pressure on the particles, this study connected the rheological frameworks of both dense dry-granular and suspension flows. Their measurements of bulk parameters remarkably showed that friction could be described as a smooth transition from the dry-granular rheology to the dilute suspension rheology (where particle-particle contacts are completely neglected):

$$\begin{aligned} \mu(I_v) &= \mu_{\text{dry}}(I_v) + \mu_{\text{susp}}(I_v) \\ &= \mu_s + (\mu_d - \mu_s)/(I_0/I_v + 1) + I_v + \frac{5}{2} \phi_c I_v^{1/2}, \end{aligned} \quad (2)$$

where $I_0 = 0.005$, $\mu_s = 0.32$, and $\mu_d = 0.7$. The values for μ_s and μ_d are in the classical range observed for dry granular flows [29, 32], while I_0 appears to depend on the definition of t_{micro} . The term ϕ_c is the packing fraction at which viscosity diverges in suspension experiments, found equal to 0.585 by Boyer *et al.* [30]. The associated

relationship of the bulk packing fraction ϕ with the viscous number was found to be:

$$\phi = \frac{\phi_c}{1 + I_v^{1/2}}. \quad (3)$$

This formalism has been validated by Boyer *et al.*[30] for a uniformly confined, sheared system. However, it has not yet been validated for conditions that are more relevant to river flows; i.e., settling particles ($\rho_p/\rho_f > 1$) where the pressure and shear-rate vary vertically. In particular, the implementation of this rheology in a two-phase model by Aussillous *et al.* [23] was not able to reproduce their experimental results. It is unclear, however, what is the source of the disagreement between $\mu(I_v)$ rheology and sediment-transport experiments. Previous studies lacked accurate measurements of, and therefore had to make assumptions about: (1) the packing fraction, and therefore pressure conditions, at the fluid-sediment interface; and (2) the movement of very slow particles deep in the bed, which were assumed to be immobile [21, 23]. Resolving the mismatch between model and data requires improved measurements of particle motion in the vicinity of the surface and deep inside the bed.

Our recent experiments showed that settling particles entrained by a laminar fluid flow exhibit three different regimes of motion as a function of depth into the bed[27]: (I) a dilute regime where particle motion is mostly driven by fluid-flow stress; (II) a denser particle flow, similar to a dry-granular flow, that we identified as bed-load; and (III) a creep regime associated with exceedingly slow and intermittent particle motion (see Fig. 1a). Particle velocity and concentration changed continuously across these regimes; however, the transition to creep seems to occur at a fixed viscous number, regardless of the applied fluid stress. Drawing on these observations, in this paper we determine the rheology of laminar sediment transport across all three regimes, and confront these results with the local rheology proposed by Boyer *et al.*[30].

II. EXPERIMENTAL SETUP AND METHODS

A. Experiment setup

Technical details of the experiments performed were presented in Houssais *et al.* [27], so we only briefly review them here. The setup consists of a closed annular flume of radius $R = 17$ cm, in which we submerge a layer of spherical acrylic particles of diameter $d = 1.5$ mm and density $\rho_p = 1190$ kg/m³ in an oil of viscosity $\eta_f = 68.6 \eta_{water}$ and density $\rho_f = 1050$ kg/m³ (see Fig. 2). The system has width $W = 17d$, depth $H = 14d$, and is sheared by rotating the top of the flume at a constant rate Ω (from 0.8 to 4 rpm) which corresponds to a top plate velocity, $U = 2\pi R\Omega$ (from 14 and 48 mm/s). Below the plate is a fluid gap with a flow depth h_f , which is measured

and ranges from 3.8 to 5.6 mm. The low Reynolds numbers ($Re = \rho_f h_f U / \eta_f \leq 3$) and low aspect ratio h_f/W act to suppress turbulence and secondary flows [1]. The bottom and side walls are smooth, which allows particle slip at the boundaries (visible on movie 1 of Houssais *et al.* [27] Supplementary Information). Some slip is inevitable in granular flow experiments [36]; we believe this slip is a feature for our experiments, that limits the influence of the bottom boundary on particle motion in the pack. To visualize granular dynamics, we index-match the PMMA particles with a viscous oil (85% of PM550 and 15% of PM556 from Dow Corning, as previously used[37]), and record fluorescence of a dye (Exciton, pyrromethene 597) dispersed in the fluid and excited with a green laser sheet (517 nm, 50 mW) of thickness $\simeq d/10$ (ref. [38]) aligned with the middle of the channel width (see Fig. 2b). Therefore, we image a vertical plane that is farthest from the influence of the side walls.

The granular bed is prepared for each experiment with the following protocol: for 5 minutes the flume top is rotated at 3 rpm, applying a shear stress strong enough to suspend all particles, except the two bottom layers at the bottom which crystallize. The rotation then slowly returns to zero, and the particles settle for 5 minutes, building a random packed bed of approximately $11d$. Then, a constant rotation Ω of the top plate drives the system during the entire experiment. The duration of the experiment is not fixed; each lasts long enough (10 hours to several days) that all particles present in the recorded frames exhibit detectable displacement during the run. With a single camera two different records are acquired: 20-min long movies with a frame rate of 30 Hz, able to capture particle flights at the surface, and hours-long time-lapse at 0.067 Hz, able to capture slow creeping motion deep inside the bed.

B. Analysis

To compute particle positions and apparent size, each recorded image is processed in the following manner. First, a convolution with a disk of a radius close to that of a particle filters most of the image noise. Second, a radial symmetry analysis is made at each pixel, to reveal particle center positions as the most symmetrical objects. Finally, for each of these positions the average distance to the particle boundary (obtained from a binary version of the raw image) is taken as the apparent radius of the particle (see result example Fig. 2d).

Vertical profiles of particle concentration are computed from the image of the detected particle areas, by averaging pixels in the x direction (see profile example Fig. 2c). We assume the particle concentration measured in a two-dimensional (2D) plane is a good proxy for the packing fraction $\phi(z)$, as our measured saturation values deep inside the bed are close to classical values found for random packing fraction (0.58 to 0.6), and close to the value of ϕ_c in equations (2) and (3). Even in the time-averaged

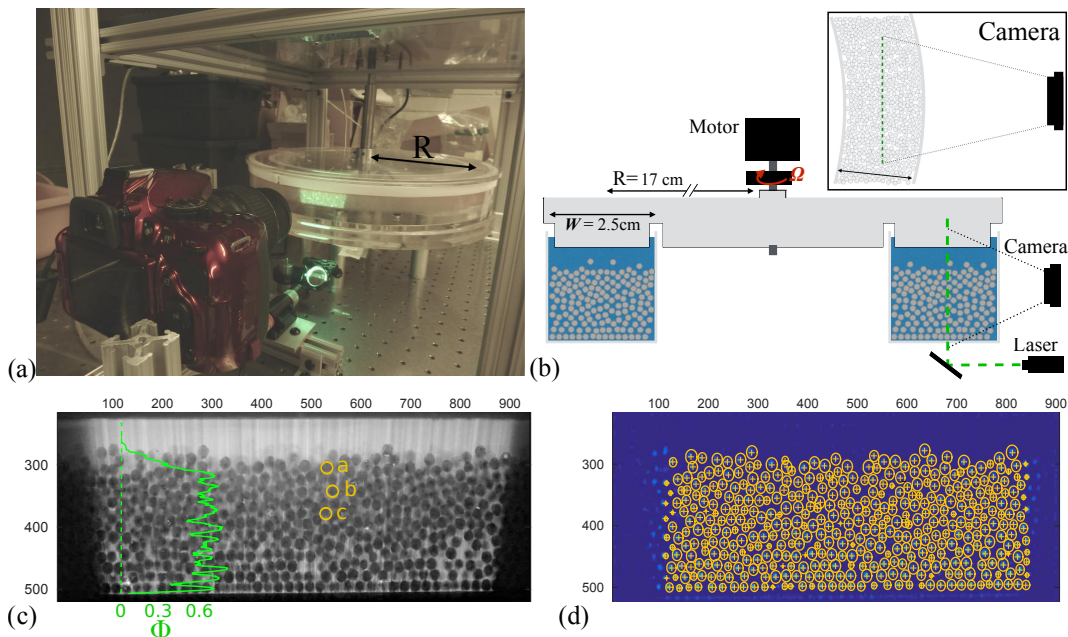


FIG. 2. Experimental setup and particle detection. a) Picture of the experiment with camera, laser and an illuminated 2D plane of particles. b) Sketch of the experimental setup, with dimensions indicated. Inset: Top view. c) Image showing 2D plane of particles. Green curve is the depth-varying packing fraction, computed at each elevation as the fraction of the image in the x -direction that is occupied by particles. The trajectories of particles highlighted here in yellow are shown in Fig. 4 d) Typical particle detection result. Experimental results correspond to a run performed at $U = 48$ mm/s.

profile, vertical oscillations of the packing fraction are present. This is related to the tendency for particles to settle in layers, and produces fluctuations with a wavelength comparable to the particle diameter that are especially notable at the bottom and the surface. Each experiment exhibits an initial phase of fast compaction, which drives a temporal evolution of ϕ . Fig. 3 presents the typical time evolution of the bed surface elevation. To study the steady-state rheology, we begin collecting data after most of the compaction has occurred (orange area on Fig. 3).

Even after the compaction stage, we observe significant fluctuations in the concentration profile from image to image due to a finite sampling window, in particular at the bed surface. Peak values for the packing fraction exceed 0.6 significantly in the vicinity of the bed surface, and are particularly high at low shear stress. We interpret this to be a consequence of the ability of the granular bed to densify at the surface under the action of gentle particle rearrangement, producing packing fraction values commonly found for 2D systems. Nevertheless, below the surficial particle layer, the concentration profile always saturates at a constant value. We compute this saturation value (for $1 < z/d < 9$), $\langle \phi_{sat} \rangle_k$ for each experiment k ($k = 1, 5$), from time-averaged profiles made from hundreds to thousands of images. We find the mean value $\langle \phi_{sat} \rangle_m = 0.589$, with slight variations (0.5 to 3% of $\langle \phi_{sat} \rangle_m$) from experiment to experiment. In order to ensure that packing fraction profiles for all experiments converge with each other at depth, we present

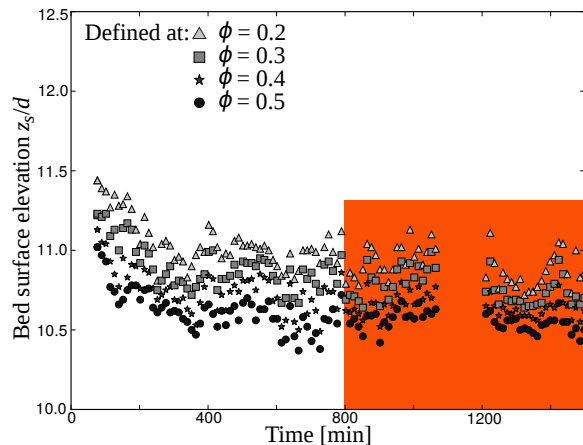


FIG. 3. Time evolution of bed surface elevations defined at different specific packing fraction ϕ , for $U = 14$ mm/s. The grey (orange online) area represents the period over which long term measurement has been performed.

k -experiment profiles normalized by $\langle \phi_{sat} \rangle_k / \langle \phi_{sat} \rangle_m$.

To compute mean particle velocity, as in Houssais *et al.* [27] we use Lagrangian particle tracking[39]. From the particle tracks, we then compute individual velocities by measuring the time difference over which particle displacements exceed a fixed probing distance $\delta x = 3d/100$. Profiles of horizontal velocity are computed by averaging elevation strips in the x direction over hours of records

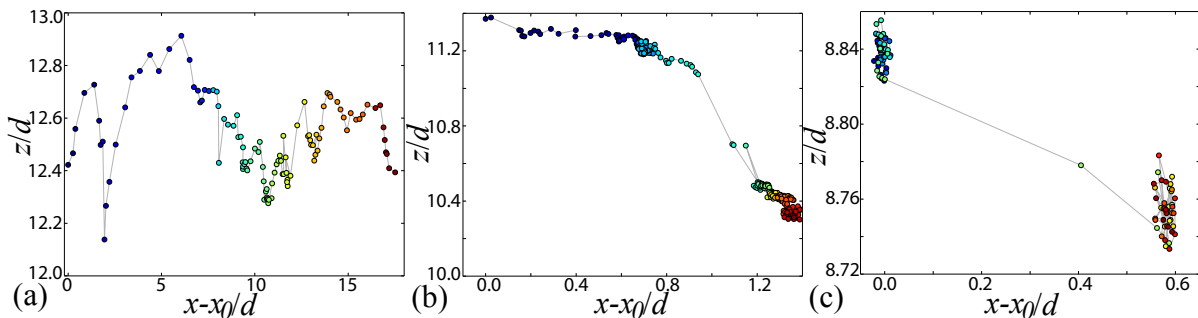


FIG. 4. Example of trajectories $z(x)$ at different elevations in the sediment bed. a) $z \simeq 11d$, b) $z \simeq 9d$, c) $z \simeq 7d$ (see positions in Fig. 2c), for the experiment performed at $U = 48$ mm/s, captured during the same 20 min movie. Color represents time, normalized by the total duration of each trajectory: a) 50 s, b) 115 s and c) 35 s, respectively. Note different axis scales for each plot. Consecutive points are all separated by 0.33 s.

(see more details in Supplementary Information of Housais *et al.* [27]).

The sediment bed is driven by a fluid and therefore there is no imposed confinement pressure; instead, there is a free-surface condition. As a consequence, the local pressure P_p increases with depth due to the increasing overburden of particles, an effect described by multiple researchers, see e.g. Jenkins and Mancini [40], as $P_p(z) = (\rho_p - \rho_f)g \int_z^{+\infty} \langle \phi \rangle dz$ where g is gravity and $\langle \phi \rangle$ is the time-averaged and horizontally ensemble-averaged packing fraction. Note that this expression implies that the confining pressure is zero at the fluid-granular interface. Several researchers [41–43] have pointed out, however, that there must exist a finite pressure acting on grains at the interface. Andreotti [44] argued that a non-zero shear-rate at the free surface of granular flows implies a non-zero confining pressure, and suggested that this could be related to the friction associated with a grain interacting with the bed. This is consistent with the notion of Johnson [42] that there is a constant (time-averaged) pressure P_0 associated with the forces acting on an individual particle at the free surface. For our experiments with sedimenting spheres driven by steady fluid shear, we expect that P_0 is a constant pressure term associated with the weight of an individual grain.

$$P_0 = (\rho_p - \rho_f)g \frac{V_g}{A_g} = \alpha (\rho_p - \rho_f)gd, \quad (4)$$

where V_g is the typical grain volume A_g is the typical grain surface area in contact with the bed, and α is the exact constant of integration. As gravity is exerted on all particles, we propose a modified confining pressure profile:

$$P_p(z) = P_0 + (\rho_p - \rho_f)g \int_z^{+\infty} \langle \phi \rangle dz. \quad (5)$$

The bed depth ($\simeq 11d$) is smaller than the channel width ($17d$), so we do not expect the confinement pressure to saturate with depth. Therefore, we do not account for the Janssen effect associated with the presence of side walls [45].

The time-averaged granular pressure (5) we propose is novel in that it includes an explicit term for single-particle force (P_0) and it incorporates the time-averaged particle pressure from suspended grains flowing above the granular bed (region I). As a consequence, this definition does not depend on whether or how the interface between the granular bed (region II) and the suspension (region I) is delineated. Below we explore the consequences of the P_0 term for modeling the local rheology of sediment transport.

III. RESULTS

A. Phenomenology and shear stress measurement

For each experiment driven at a different rotation rate, we observe the same phenomenology: the particles at the bed surface are entrained by the fluid, and present classical features of rolling and saltation, with significant velocity oscillations [1, 11, 46] (see Fig. 4a). Particles just below the surface are also transported, due to grain and fluid motion above, but their trajectories remain confined as in a granular flow (see Fig. 4b). Finally, particles deep inside the bed experience slow and sporadic motion that we identify as creep. Most of the time these particles appear to be caged [47], but occasionally they make a fast but small displacement (see Fig. 4c). The range of stresses for our experiments were all low enough that entrained particles never touched the rotating top plate, which means that the concentration of particles always drops to zero at some height above the bed [27] (see Fig. 2c). Figure 5 shows the long-time averaged profiles of packing fraction $\langle \phi \rangle$ and streamwise velocity $\langle V \rangle$ obtained for 5 experiments performed at $U = 14, 16, 21, 37$ and 48 mm/s. Velocity error bars were computed using a classical error propagation method (see details in Housais *et al.* [27]), and packing fraction error bars represent the standard errors from time averaging; due to long time averaging, error bars on $\langle V \rangle$ and $\langle \Phi \rangle$ are significantly smaller than the symbols. The concentra-

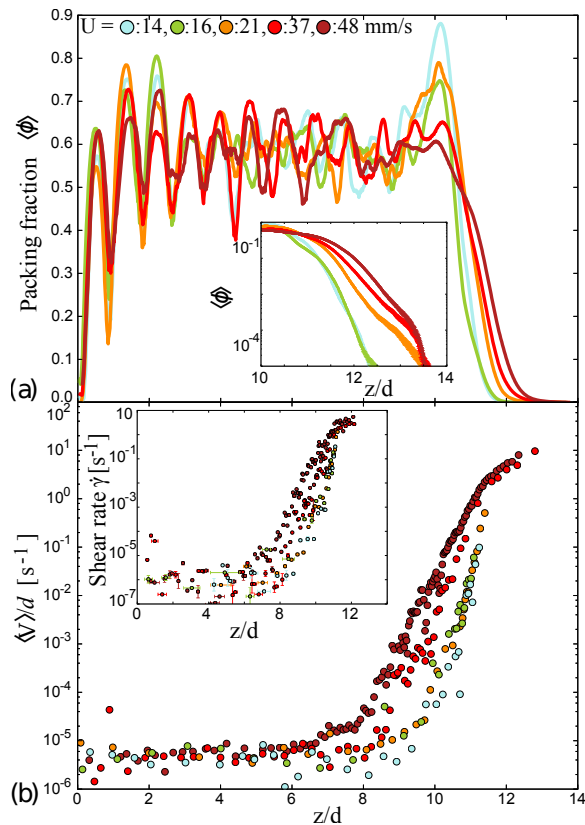


FIG. 5. Depth-dependent concentration and velocity. a) Vertical profiles of long-time averaged particle concentration. Error bars are generally smaller than the symbols and cannot be seen. Inset shows semilog plot, where error bars are visible from $\phi < 10^{-3}$. b) Vertical profiles of long-time averaged particle velocity. Inset shows its derivative, the particle shear rate $\dot{\gamma}$.

tion profiles all attain the saturation value $\langle\phi_{\text{sat}}\rangle_m$ in the lowest part of the bed, and all drop to zero moving up across the grain-fluid interface — a distance of 2 to 3 particle diameters. The inset of Figure 5a shows that these packing fraction profiles are particularly precise and well resolved for $10^{-4} < \phi < 1$. Consequently, using equation (5) we obtain high-precision pressure profiles (see examples Fig. 6), which allows us to investigate the regime where $\phi \rightarrow 0$. The term P_0 has a significant influence on the computed pressure near the bed surface, and becomes negligible below a certain depth (typically $z/d \simeq 9$ for our experiments; Fig. 6). For all stresses, one can observe that the velocity is smallest at the bottom, increases continuously with increasing z , and exhibits a significant kink at $\langle V \rangle/d \simeq 10^{-5} \text{ s}^{-1}$; the depth associated with this kink varies with the flow speed. The two highest-flow velocity experiments present a second kink in the vicinity of the surface ($z/d \simeq 11$). The fluid depth h_f is measured from $\langle\phi\rangle$ profiles $h_f = H - z_s$, where H is the total depth of the flume and z_s is the elevation at which $\langle\phi\rangle|_{z=z_s} = \langle\phi_{\text{sat}}\rangle_m/2$, an indicator of the bed surface[22]. Therefore we compute the mean fluid shear

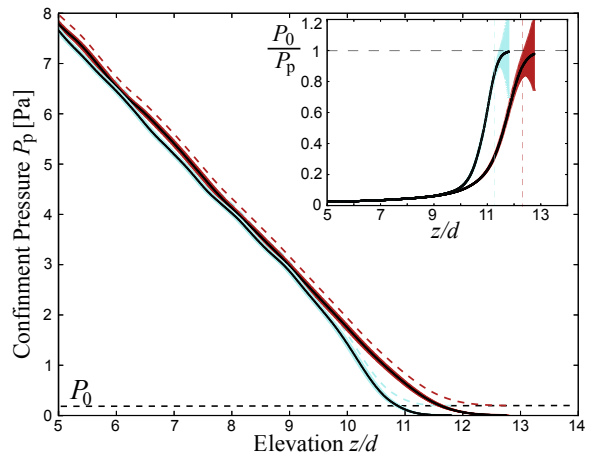


FIG. 6. Vertical profile of the confinement pressure P_p in the system for $U = 14$ mm/s (light grey, blue online) and $U = 48$ mm/s (dark grey, red online). Solid lines are the profiles obtained using $P_0 = 0$, where error bars are represented. Dashed lines are the same profiles, using $P_0 = 0.19$ Pa; for clarity, error bars are not represented. Inset: vertical profile of the ratio of $\frac{P_0}{P_p}$, using $P_0 = 0.19$ Pa, with error bars. The light and dark grey (blue and red online) dashed lines represent respectively the positions of the highest measurement of the shear rate $\dot{\gamma}$ for $U = 14$ mm/s and $U = 48$ mm/s.

stress in the region $z_s \leq z < H$ at steady state, and assume it to be a close estimate of the total shear stress τ applied on the system:

$$\tau = \eta_f \frac{U - \langle V \rangle|_{z=z_s}}{h_f} \quad (6)$$

where $\langle V \rangle|_{z=z_s}$ is the mean particle velocity measured at z_s . Our calculation of τ differs from previous studies[1, 21, 25] in that we define the bed surface from the concentration profile, and that we take into account the slip velocity of particles at the surface. Although h_f can vary $\pm 1 d$ depending on the choice of $\langle\phi\rangle$ that defines the bed surface, we note that $\langle V \rangle|_{z=z_s}$ also varies with $\langle\phi\rangle$ in a manner that partially compensates. We explicitly compute this sensitivity of τ on how we define z_s and find the dependence is mild; for two extreme bed surface definitions, determined at $\langle\phi\rangle = 0.55$ and $\langle\phi\rangle = 0.05$, the computed stresses are respectively 20 % smaller and 20 % larger for the highest shear stress experiment. We emphasize these are strict upper limits on the uncertainty of τ . This difference drops to 5 % for the lowest shear stress experiment.

For sediment transport studies it is common to normalize the shear stress by a normal stress due to the particle weight, to compute the Shields number:

$$\tau^* = \frac{\tau}{(\rho_p - \rho_f)gd}. \quad (7)$$

As we increase τ^* and the sediment transport rate increases, the width of the transition from the quasi-static

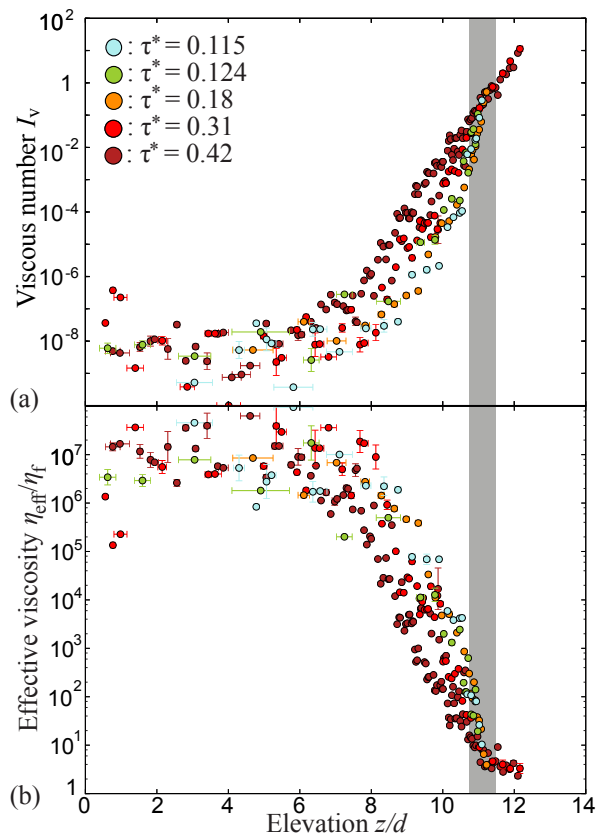


FIG. 7. Vertical profiles of long-time averaged a) viscous number and b) effective viscosity, computed using $P_0 = 0$. The gray area represents the range of elevations where concentration profiles $\langle \phi \rangle(z) = \langle \phi_{sat} \rangle_m / 2$, an estimate of the bed surface locations.

bed to the fluid — where the particle concentration drops — becomes broader (see Fig. 5a).

B. Rheology using $P_0 = 0$

As discussed in the Introduction, a major difference between the local rheology model developed and applied in the experimental system of Boyer *et al.* [30], and a sediment transport system with a free surface, is the treatment of the pressure. Instead of a constant confining pressure applied from the container, there is a depth-varying pressure that results from the weight of the grains. Previous experimental sediment-transport studies have employed the local rheology model with depth-varying pressure [23, 48], but they did not include the pressure term P_0 proposed here. To understand the significance of this additional term, we examine granular rheology first by assuming $P_0 = 0$, the simplest hypothesis. In the next subsection we compare these findings to results that include a non-zero P_0 value. Fig. 7a shows the profiles of viscous number I_v , computed from the packing fraction and velocity profiles. Interestingly, on one hand, as already showed by Houssais *et al.* [27], the

velocity kink deep in the bed corresponds to a viscous number kink at $I_v \simeq 10^{-7}$. But on the other hand, all the profiles appear to converge to $I_v \simeq 1$ close to the surface. This observation is consistent with the expectation that a dynamical transition from the granular regime to the suspension regime occurs as I_v approaches 1 [30]. This is supported by the behavior of the effective viscosity η_{eff} , which saturates at high packing fraction at a value $\simeq 10^7 \eta_f$; in the other limit, all profiles converge to $\eta_{eff} \simeq 3\eta_f$ at the surface as the concentration decreases toward zero (Fig. 7b). Notably, for the two highest stresses η_{eff} profiles continue to decay toward η_f ; i.e., the effective viscosity is determined only by the fluid. Taken together, data show the appropriate limits and indicate that sediment transport undergoes a transition from a dense granular material to a suspension.

In Figures 8 and 9 we compare our dimensionless local measurements of ϕ , I_v , η_{eff} and μ with the extended local granular rheology proposed by Boyer *et al.* [30]. One can see that the data are broadly consistent with the model (Fig. 8), as they cluster around the relations from equations (2) and (3). The data, however, deviate from model predictions as ϕ decreases, and also appear to exhibit different ϕ values at the deviation for different Shields stresses (from $\phi \simeq 0.57$ for $\tau^* = 0.115$ to $\phi \simeq 0.32$ for $\tau^* = 0.42$). As our packing fraction profiles are well resolved for $\phi > 10^{-4}$, these deviations from the model are not due to measurement error and are therefore significant. The deviation is similarly apparent for the local effective friction coefficient $\mu = \tau/P_p(I_v)$ (Fig. 9). For values $I_v > 3 \times 10^{-5}$, the deviation of μ from the rheology model becomes more severe as the Shields number decreases. Moreover, μ grows to unphysically large values, especially considering that as $\tau^* \rightarrow \tau_c^*$ the behavior should approach a quasi-static limit. We interpret this effect to be the result of a systematic bias, that arises due to the lack of the constant pressure P_0 , which carries more and more of the normal stress as particles reach the interface with the clear fluid.

C. Rheology using $P_0 = \alpha(\rho_p - \rho_f)gd$

The assumption of $P_0 = 0$, or $\alpha = 0$, results in unphysical behavior at the surface, and does not produce a collapse of our experimental data. Potential errors in our estimation of shear stress are not sufficient to explain the deviation of μ from model predictions. In particular, the deviation of μ data from equation 2 near the surface increases as shear stress decreases, i.e., where errors in estimates of the shear stress τ are minimal. Because particles are settling, there exists a finite elevation where the packing fraction drops to zero (Fig. 1a). Accordingly, if $P_0 = 0$, the viscous number diverges to infinity in the dilute region ($\langle \phi \rangle \ll 1$). We tested different P_0 values, and found a reasonably good collapse for plots of μ vs I_v for $0.16 \text{ Pa} \leq P_0 \leq 0.23 \text{ Pa}$. The data presented in subsequent figures are computed with $P_0 = 0.19 \text{ Pa}$,

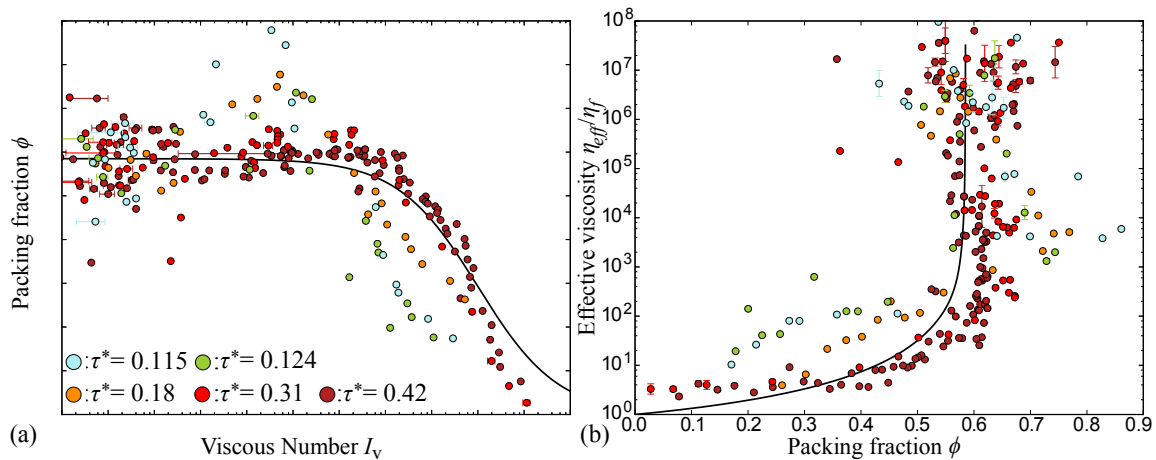


FIG. 8. a) Long-time averaged particle concentration as a function of the viscous number (computed using the confining pressure P_p). Black line represents equation (3). b) Long-time averaged effective viscosity η_{eff} as a function of the concentration. Black line represents the effective viscosity relationship with packing fraction resulting from equations (2) and (3). Both plots computed using $P_0 = 0$.

or $\alpha = 0.1$. Including the pressure term P_0 has several important consequences. First, local measurements from all our experiments collapse onto a single $\mu(I_v)$ curve for $I_v \geq 3 \times 10^{-5}$ (Fig. 10). In other words, the rheology becomes independent of Shields stress. Second, these data cluster very close to the local rheology model prediction over the range of collapse. Third, the friction coefficient does not diverge indefinitely in the high I_v limit. Instead, the effective friction coefficient μ converges toward a finite value of $\mu = \tau/P_0$ associated with the clear-fluid limit $\phi = 0$. Fourth, the value of P_0 is physically meaningful as it is of the same order of magnitude as the normal stress due to the weight of a single spherical particle ($\simeq (\rho_p - \rho_f)gd/3$), which confirms the validity of equation (5). The effect of P_0 on the computed pressure profile is negligible deep in the bed, but becomes more significant on approach to the surface (Fig. 6).

Importantly, the existence of the positive term P_0 is consistent with the existence of a critical stress τ_c for onset of particle entrainment and the asymptotic behavior of static friction. Indeed, as τ approaches τ_c , μ approaches μ_s at the bed surface [5, 6]. Therefore, the critical stress to entrain a particle resting on the bed surface is naturally set as $\tau_c = \mu_s P_0$ (see Fig. 1b). As our experiments have been performed with PMMA spherical particles, similar to those used by Boyer *et al.* [30], we used the same value for $\mu_s = 0.32$ to compute τ_c . We found, for the range of P_0 cited above, $0.05 \text{ Pa} \leq \tau_c \leq 0.07 \text{ Pa}$, which corresponds to a range of critical Shields number $0.025 \leq \tau_c^* \leq 0.035$. Fig. 10 is made with $\tau_c^* = 0.03$.

Finally, a remarkable finding is that, for $I_v < 3 \times 10^{-5}$, the data do not show convergence of the friction coefficient with the static value ($\mu = \mu_s$). Instead, μ decays continuously below μ_s with decreasing I_v , and the different experimental curves deviate from each other for values $\mu < \mu_s$. We do not observe any saturation of these trends.

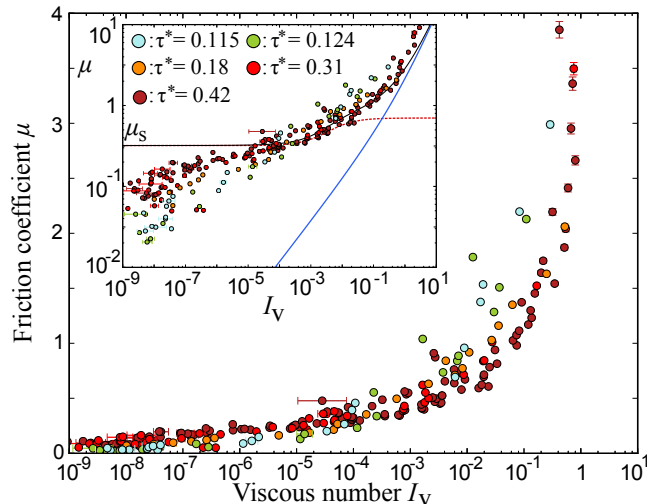


FIG. 9. Friction coefficient μ as function of I_v , computed using $P_0 = 0$. Inset shows the logarithm of μ , where the dashed (red online) and full (blue online) grey lines represent $\mu_{\text{dry}}(I_v)$ and $\mu_{\text{susp}}(I_v)$ respectively, and the black line represents equation (2).

IV. DISCUSSION

In the Boyer *et al.* [30] experiment, a single flow state associated with a single bulk viscous number was observed at a time, under an imposed confining pressure and packing fraction, and for the range: $10^{-6} < I_v < 0.2$. For our system, the local shear rate and packing fraction adjust dynamically to the imposed fluid stress because of the free-surface condition. This results in a depth-varying viscous number and, as a result, multiple flow regimes coexist over the range: $10^{-9} < I_v < 2$. Despite these differences, we find that the $\mu(I_v)$ rheology

proposed by Boyer *et al.*[30] can be extended to the case of settling particles sheared from above by a fluid, with the addition of a pressure term $P_0 \simeq 0.1(\rho_p - \rho_f)gd$ that accounts for particle weight. Our data closely follow the model for the range $3 \times 10^{-5} \leq I_v \leq 2$. For indication, a best fit (dashed line on Fig. 10) over that specific range of the data gives the parameters : $I_0 = 0.0012 \pm 0.0004$, $\mu_s = 0.27 \pm 0.01$ and $\mu_d = 0.52 \pm 0.02$. This result shows that a single rheology is capable of describing the complex case of sediment transport from bed load to suspension, as a transition from a slow and dense to a fast and dilute granular flow. This sediment transport regime is bounded by a fluid flow above where particle concentration vanishes, and a creeping granular system below where the local rheology model breaks down.

The success of the pressure term P_0 in collapsing the data and recovering the rheology prediction confirms that this is a physically-meaningful term, and that the sediment-fluid interface has to be treated specifically as a pressure boundary condition. Also, the inferred value for $t_{\text{micro}} = 0.37$ s from P_0 is of the same order as the particle free-fall timescale $d/V_s = 1.2$ s, where $V_s = g(\rho_p - \rho_f)d^2/(18\eta_f)$ is the Stokes velocity. Our results moreover suggest a new method for assessing the critical stress τ_c from dynamics, which is quite different from the usual approach that extrapolates the flux-stress relation to zero. Our inferred value $\tau_c^* = 0.03$ is low relative to previous studies in laminar flow, where reported values are typically twice as large [1, 49]. Nonetheless, it is compatible with the very sparse particle motion we observed at the surface during an experiment performed at $\tau^* = 0.043$ (see movie 3 in Supplementary information of Houssais *et al.* [27]). It is also close to the value reported by Charru *et al.* [1] at the start of their experiments ($\tau^* = 0.04$) — before any compaction occurred — where entrainment of loose surface particles may approximate the situation of a single grain resting on the bed (Fig. 1b).

It appears that the critical condition for motion of an individual particle on the bed surface may be characterized by a static friction threshold through τ_c^* . The $\mu(I_v)$ rheology, however, indicates that τ_c^* does not represent a well-defined yield stress criterion for the granular surface, instead $\mu = \mu_s$ defines the interface with the quasi-static dense bed. This is consistent with observations of creep behavior in dry granular material in horizontal shear experiments [50–52]. Our results generally support recent studies calling for a modification to the classical bed-load transport framework; in particular, that the friction coefficient cannot be considered constant [21, 22], and that the “bed-load active layer” is not constant but instead expands vertically in both directions as the shear stress τ increases [22]. Results also inform models for suspended-sediment transport, supporting the idea of Boyer *et al.* [30] that particle-particle frictional interactions should be taken into account, even for smooth spheres suspended in a viscous fluid. Interestingly, a similar reasoning has been developed recently in order to understand shear thicken-

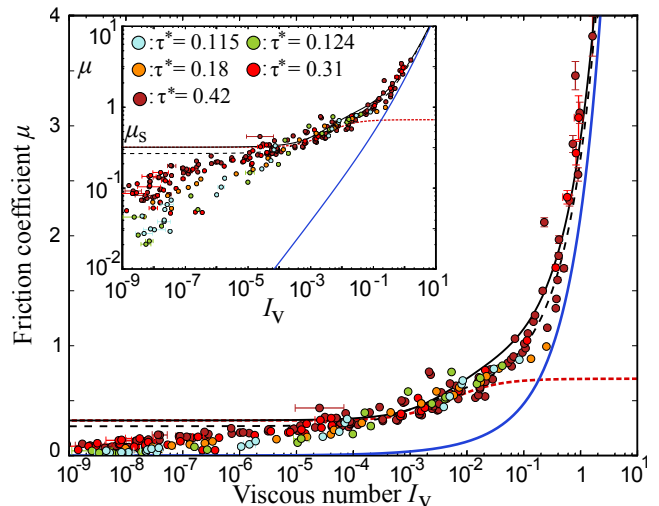


FIG. 10. Friction coefficient μ as function of I_v , computed using the confining pressure $P_0 \simeq 0.1(\rho_p - \rho_f)gd$ that accounts for particle weight. Inset shows the logarithm of μ . The dashed (red online) and full (blue online) grey lines represent $\mu_{\text{dry}}(I_v)$ and $\mu_{\text{susp}}(I_v)$ respectively, and the black line represents equation (2). The black dash line represents a best fit on the data over the range $3 \times 10^{-5} \leq I_v \leq 2$, using equation (2), where ϕ_c is the only fixed parameter.

ing in suspensions [53, 54]. This suggests that improvements in our understanding of particle-scale interactions may yield a local rheology model capable of describing granular flows across a broad range of packing fraction and shear stress conditions.

Some models have utilized a closure scheme in which granular transport ceases at a critical packing fraction [24, 55], however our experiments show that this is not the case. This raises an important issue: the rheological picture presented here is still incomplete, as there is no prediction for the packing fraction profile itself. This was measured rather than modeled in our study. However, our packing fraction data – validated by our finding of the $\mu(I_v)$ relationship – show that these profiles deviate from the classical rheology prediction (equation 3). Suspension modeling studies have proposed that particle diffusion due to internal pressure induces a flux normal to the shear [30, 56], and that the competition between diffusion and particle settling may be used to determine the sediment concentration profile [24]. This, however, remains to be fully validated. To be relevant for sediment transport, we propose that any closure equation for the concentration profile should also be consistent with the condition of a quasi-static bed at $\tau^* = \tau_c^*$.

Finally, our results identify two regime transitions where the local rheology breaks down. As we mentioned above, the first one corresponds to where the packing fraction data deviate from the $\phi(I_v)$ relationship (see Fig. 8). The second important transition occurs for $I_v < 3 \times 10^{-5}$, where data from different experiments deviate from the model and each other. Based on obser-

vations of particle motion [27], we interpret this deviation as the signature of the creep regime. Creep is associated with values $\mu < \mu_s$, where μ continues to decline with decreasing I_v . The local rheology model predicts that μ converges to μ_s for vanishing I_v , representing a jamming transition [24, 29, 30]. Our experiments, which reach values for I_v more than three orders of magnitude smaller than reported in Boyer *et al.* [30] study, do not show any jamming transition.

It is important to note that creep is associated with localized, intermittent particle motion such that the average particle velocity profile – and so μ versus I_v – may be less directly related to the relevant dynamics. It is likely that the assumption of strictly local particle interactions is broken for creep, where collective particle motion may be expected to occur [57] and long-range interactions due to force chains may be relevant. New experiments dedicated to creep should be conducted, with a focus on resolving the very long-time and large-space scales required to determine particle trajectories. Although our experiments are limited to a single type of particle, fluid and boundary condition, we are able to explore a very wide range of viscous number. It is possible that changes in the fluid, sediment or boundary parameters may cause deviations from our findings. More exploration of these effects is needed, however the use of refractive-index matching limits the possible combinations of fluid and sediment. In addition, our channel geometry limits our ability to explore different grain sizes. Nevertheless, previous studies with varied particle size and fluid viscosity [11, 23, 30] lead us to believe that our findings are robust for $I_v > 3 \times 10^{-5}$. While the transition to creep occurs at a constant critical I_v value for our experiments, further study is needed to determine if this number is robust and to examine its physical meaning. In particular, it may be useful to vary the channel geometry (flume curvature versus channel width) and boundary conditions (roughness amplitude versus the particle size) in laboratory experiments.

In term of analysis, future examination of dynamical heterogeneities in the experimental data will help to address the rheology break down. From the theoretical side, the recent development of a non-local rheology framework [58–60] is a promising approach for modeling creep dynamics. Currently, predictions from non-local models appear to be inconsistent with our observations [61], as they predict deviation from the local rheology at large viscous number. Results cannot be directly compared at present, however, as the non-local models implement a boundary condition of no particle motion very far from the shear zone. The few experiments where creep has

been quantified [27, 50–52] used varying boundary conditions (from smooth to rough), but some boundary slip likely occurred for all conditions [36]. If creep is indeed driven by non-local dynamics, varying boundary conditions in non-local rheology models will allow for insightful comparisons with different experimental results that will enrich our understanding of the creep mechanism.

V. CONCLUSION

Performing a laminar-flow experiment with very-highly resolved particle detection, we capture the rheology of sediment transport across the full range of behavior — from quasi-static creep, to the dense-granular flow associated with bed load, to dilute suspension. Quantifying the constant pressure term P_0 , which is a fraction of the normal stress due to the weight of an individual particle, we can then link the classical definition of critical shear stress τ_c to the local rheology of a granular flow submerged in a viscous fluid. These results provide a new perspective on the modeling of sediment transport processes with continuum mechanics, and open the possibility that creeping to suspension regimes — which are responsible for most of landscape dynamics — may be described with a unified rheology. Our results emphasize the importance of the pressure P_0 near the bed surface. The effect of this parameter may be relevant for transport and segregation of mixed grain sizes in submerged granular flows. Finally, the transition to creep at low viscous number challenges our understanding of local rheology and the nature of the jamming transition. At present we have an incomplete understanding of the packing fraction near the free surface and the motion of particles in the creep regime deserve; these deserve further investigations that may motivate new comparisons with non-local rheology models. Many rivers and hillslopes are granular systems that self-organize such that they are in the vicinity of the threshold of motion [62]. Thus, a better understanding of creep dynamics will improve long-term predictions of landscape evolution.

Acknowledgments: Research was supported by US Army Research Office - Division of Earth Materials and Processes grant 64455EV, and US National Science Foundation grants EAR-1224943 and INSPIRE/EAR-1344280, to D.J.J.; and MRSEC/DMR-1120901 to D.J.D. We thank R. L. Martin for his contribution to the initial design of the experimental apparatus, and Jeff Hancock and Harold Borders for technical support. M. H. thanks Jeffrey F. Morris for insightful discussions on the meaning and consequences of P_0 .

[1] F. Charru, H. Mouilleron, and O. Eiff, *J. Fluid Mech.* **519**, 55 (2004).
 [2] L. Malverti, E. Lajeunesse, and F. Metivier, *J. Geophys. Res.* **113**, F04004 (2008).

[3] E. Lajeunesse, L. Malverti, P. Lancien, L. Armstrong, F. Métivier, S. Coleman, C. E. Smith, T. Davies, A. Cantelli, and G. Parker, *Sedimentology* **57**, 1 (2010).
 [4] M. D. Reitz, D. J. Jerolmack, and J. B. Swenson, *Geo-*

- physical Research Letters **37** (2010).
- [5] I. A. Shields, *Mitt. Preuss Ver.-Anst.* **26** (1936).
- [6] P. L. Wiberg and J. D. Smith, *Water Resour. Res.* **23**, 1471 (1987).
- [7] J. M. Buffington and D. R. Montgomery, *Water Resour. Res.* **33**, 1993 (1997).
- [8] P. R. Wilcock and J. C. Crowe, *J. Hydraul. Eng.* **129**, 120 (2003).
- [9] M. Houssais and E. Lajeunesse, *J. Geophys. Res.* **117**, F04015 (2012).
- [10] E. Meyer-Peter and R. Müller, in *Proc. 2nd Meet. Int. Assoc. Hydraul. Struct. Res.* (International Association of Hydraulic Research Delft, 1948) pp. 39–64.
- [11] E. Lajeunesse, L. Malverti, and F. Charru, *J. Geophys. Res.* **115**, F04001 (2010).
- [12] J. C. Roseberry, M. W. Schmeeckle, and D. J. Furbish, *J. Geophys. Res.* **117**, F03032 (2012).
- [13] O. Devauchelle, L. Malverti, E. Lajeunesse, P.-Y. Lagrée, C. Josserand, and K.-D. N. Thu-Lam, *Journal of Fluid Mechanics* **642**, 329 (2010).
- [14] G. Parker, *J. Fluid Mech.* **89**, 127 (1978).
- [15] C. Paola, P. L. Heller, and C. L. Angevine, *Basin Research* **4**, 73 (1992).
- [16] G. Seizilles, O. Devauchelle, E. Lajeunesse, and F. Métivier, *Physical Review E* **87**, 052204 (2013).
- [17] J. M. Turowski, A. Badoux, and D. Rickenmann, *Geophys. Res. Lett.* **38**, L04401 (2011).
- [18] L. Hsu, N. J. Finnegan, and E. E. Brodsky, *Geophysical Research Letters* **38** (2011).
- [19] A. Recking, F. Liébault, C. Peteuil, and T. Jolimet, *Earth Surf. Process. Landforms* **37**, 774 (2012).
- [20] P. Frey and M. Church, *Earth Surf. Process. Landforms* **36**, 58 (2011).
- [21] M. Ouriemi, P. Aussillous, and E. Guazzelli, *J. Fluid Mech.* **636**, 295 (2009).
- [22] O. Durán, B. Andreotti, and P. Claudin, *Phys. Fluids* **24**, 103306 (2012).
- [23] P. Aussillous, J. Chauchat, M. Pailha, M. Médale, and E. Guazzelli, *J. Fluid Mech.* **736**, 594 (2013).
- [24] F. Chiodi, P. Claudin, and B. Andreotti, *J. Fluid Mech.* **755**, 561 (2014).
- [25] T. Revil-Baudard, J. Chauchat, D. Hurther, and P.-A. Barraud, *Journal of Fluid Mechanics* **767**, 1 (2015).
- [26] A. H. Clark, M. D. Shattuck, N. T. Ouellette, and C. S. O’Hern, *Physical Review E* **92**, 042202 (2015).
- [27] M. Houssais, C. P. Ortiz, D. J. Durian, and D. J. Jerolmack, *Nature Communications* **6** (2015).
- [28] C. Ancey, P. Coussot, and P. Evesque, *Journal of Rheology* **43**, 1673 (1999).
- [29] G. MiDi, *Eur. Phys. J. E* **14**, 341 (2004).
- [30] F. Boyer, E. Guazzelli, and O. Pouliquen, *Phys. Rev. Lett.* **107**, 188301 (2011).
- [31] P. Jop, Y. Forterre, and O. Pouliquen, *Journal of Fluid Mechanics* **541**, 167 (2005).
- [32] P. Jop, Y. Forterre, and O. Pouliquen, *Nature* **441**, 727 (2006).
- [33] Y. Forterre and O. Pouliquen, *Annu. Rev. Fluid Mech.* **40**, 1 (2008).
- [34] S. C. du Pont, P. Gondret, B. Perrin, and M. Rabaud, *Physical review letters* **90**, 044301 (2003).
- [35] C. Cassar, M. Nicolas, and O. Pouliquen, *Phys. Fluids* **17**, 103301 (2005).
- [36] P. Jop, *Comptes Rendus Physique* **16**, 62 (2015).
- [37] M. Stöhr, K. Roth, and B. Jähne, *Experiments in Fluids* **35**, 159 (2003).
- [38] J. a. Dijkstra, F. Rietz, K. a. Lorincz, M. van Hecke, and W. Losert, *Rev. Sci. Instrum.* **83**, 011301 (2012).
- [39] N. T. Ouellette, H. Xu, and E. Bodenschatz, *Exp. Fluids* **40**, 301 (2005).
- [40] J. T. Jenkins and F. Mancini, *Journal of Applied Mechanics* **54**, 27 (1987).
- [41] S. B. Savage, *Journal of Engineering Mathematics* **60**, 221 (2008).
- [42] P. Johnson, P. Nott, and R. Jackson, *Journal of Fluid Mechanics* **210**, 501 (1990).
- [43] P. C. Johnson and R. Jackson, *Journal of Fluid Mechanics* **176**, 67 (1987).
- [44] B. Andreotti, *Europhysics Letters (EPL)* **79**, 34001 (2007).
- [45] G. Ovarlez, C. Fond, and E. Clément, *Phys. Rev. E* **67**, 060302 (2003).
- [46] J. Abbott and J. Francis, *Phil. Trans. R. Soc. Lond. A* **248**, 225 (1977).
- [47] P. M. Reis, R. A. Ingale, and M. D. Shattuck, *Physical review letters* **98**, 188301 (2007).
- [48] T. Revil-Baudard, J. Chauchat, D. Hurther, and P.-A. Barraud, *Journal of Fluid Mechanics* **767**, 1 (2015).
- [49] M. Ouriemi, P. Aussillous, M. Médale, Y. Peysson, and E. Guazzelli, *Phys. Fluids* **19**, 61706 (2007).
- [50] K. Nichol, A. Zanin, R. Bastien, E. Wandersman, and M. van Hecke, *Phys. Rev. Lett.* **104**, 078302 (2010).
- [51] K. A. Reddy, Y. Forterre, and O. Pouliquen, *Phys. Rev. Lett.* **106**, 108301 (2011).
- [52] A. Pons, A. Amon, T. Darnige, J. Crassous, and E. Clément, *Physical Review E* (2015).
- [53] M. Wyart and M. Cates, *Physical review letters* **112**, 098302 (2014).
- [54] R. Mari, R. Seto, J. F. Morris, and M. M. Denn, *Journal of Rheology* **58**, 1693 (2014).
- [55] M. Trulsson, B. Andreotti, and P. Claudin, *Phys. Rev. Lett.* **109**, 118305 (2012).
- [56] D. Leighton and A. Acrivos, *Journal of Fluid Mechanics* **181**, 415 (1987).
- [57] H. Katsuragi, a. R. Abate, and D. J. Durian, *Soft Matter* **6**, 3023 (2010).
- [58] E. Lerner, G. Düring, and M. Wyart, *Proceedings of the National Academy of Sciences* **109**, 4798 (2012).
- [59] M. Bouzid, M. Trulsson, P. Claudin, E. Clément, and B. Andreotti, *Phys. Rev. Lett.* **111**, 238301 (2013).
- [60] K. Kamrin and D. L. Henann, *Soft matter* **11**, 179 (2015).
- [61] K. Kamrin and G. Koval, *Physical Review Letters* **108**, 178301 (2012).
- [62] D. J. Jerolmack, *EOS, Trans. AGU* **92**, 385 (2011).